Nuclear Instruments and Methods in Physics Research A 817 (2016) 85–92

Contents lists available at ScienceDirect

Nuclear Instruments and Methods in Physics Research A

journal homepage: www.elsevier.com/locate/nima

Performance of a full-size small-strip thin gap chamber prototype for the ATLAS new small wheel muon upgrade

A. Abusleme [c], C. Bélanger-Champagne [b], A. Bellerive [a], Y. Benhammou [f], J. Botte [a], H. Cohen [f], M. Davies [f], Y. Du [k], L. Gauthier [i], T. Koffas [a], S. Kuleshov [h], B. Lefebvre [b], C. Li [k], N. Lupu [e], G. Mikenberg [l], D. Mori [d], J.P. Ochoa-Ricoux [c], E. Perez Codina [g,m], S. Rettie [g,j], A. Robichaud-Véronneau [b], R. Rojas [h], M. Shoa [l], V. Smakhtin [l], B. Stelzer [d,*], O. Stelzer-Chilton [g], A. Toro [h], H. Torres [d], P. Ulloa [h], B. Vachon [b], G. Vasquez [h], A. Vdovin [e], S. Viel [g], P. Walker [c], S. Weber [a], C. Zhu [k]

[a] Carleton University, 1125 Colonel By Drive, Ottawa, ON, Canada, K1S 5B6
[b] McGill University, Ernest Rutherford Physics Bldg., 3600 Rue University, Montreal, QC, Canada, H3A 2T8
[c] Pontificia Universidad Catolica de Chile, Vicuña Mackenna 4860, Santiago 7820436, Chile
[d] Simon Fraser University, 8888 University Drive, Burnaby, BC, Canada, V5A 1S6
[e] Technion - Israel Institute of Technology (IIT), Haifa 32000, Israel
[f] Tel-Aviv University, Ramat Aviv, Tel Aviv 69978, Israel
[g] TRIUMF, 4004 Wesbrook Mall, Vancouver, BC, Canada, V6T 2A3
[h] Universidad Tecnica Federico Santa Maria, Casilla 110-V, Avda. Espana 1680, Valparaiso, Chile
[i] Université de Montréal, C.P. 6128, Succ. centre-ville, Montréal, QC, Canada, H3C 3J7
[j] University of British Columbia, 6224 Agricultural Road, Vancouver, BC, Canada, V6T 1Z1
[k] Shandong University, Jinan, Shandong, China
[l] Weizmann Institute of Science, Rehovot 76100, Israel
[m] CERN, CH-1211 Geneve 23, Switzerland

ARTICLE INFO

Article history:
Received 5 November 2015
Received in revised form
12 January 2016
Accepted 25 January 2016
Available online 3 February 2016

Keywords:
LHC
ATLAS upgrade
Muon spectrometer
Gaseous detectors
Tracking
Trigger

ABSTRACT

The instantaneous luminosity of the Large Hadron Collider at CERN will be increased up to a factor of five with respect to the present design value by undergoing an extensive upgrade program over the coming decade. The most important upgrade project for the ATLAS Muon System is the replacement of the present first station in the forward regions with the so-called New Small Wheels (NSWs). The NSWs will be installed during the LHC long shutdown in 2019/2020. Small-Strip Thin Gap Chamber (sTGC) detectors are designed to provide fast trigger and high precision muon tracking under the high luminosity LHC conditions. To validate the design, a full-size prototype sTGC detector of approximately $1.2 \times 1.0\ m^2$ consisting of four gaps has been constructed. Each gap provides pad, strip and wire readouts. The sTGC intrinsic spatial resolution has been measured in a 32 GeV pion beam test at Fermilab. At perpendicular incidence angle, single gap position resolutions of about 50 μm have been obtained, uniform along the sTGC strip and perpendicular wire directions, well within design requirements. Pad readout measurements have been performed in a 130 GeV muon beam test at CERN. The transition region between readout pads has been found to be 4 mm, and the pads have been found to be fully efficient.

© 2016 The Authors. Published by Elsevier B.V. This is an open access article under the CC BY license (http://creativecommons.org/licenses/by/4.0/).

1. Introduction

The motivation for the luminosity upgrade of the Large Hadron Collider (LHC) is to precisely study the Higgs sector and to extend the sensitivity to new physics to the multi-TeV range. In order to achieve these goals the ATLAS experiment [1] has to maintain its capability to trigger on moderate momentum leptons under more challenging background conditions than those present at the LHC during Run-1 and Run-2. For the Muon Spectrometer (MS) [2], such requirements necessitate the replacement of the forward muon-tracking region called the muon Small Wheel, with new detectors capable of triggering and precision tracking simultaneously. The New Small Wheel (NSW) upgrade [3] is designed to cope with the high background rate (up to 15 kHz/cm^2) that is expected at luminosities between 2 and $7 \times 10^{34}\ cm^{-2}\ s^{-1}$ during Run-3 and the high luminosity LHC (HL-LHC) runs [4].

Small-Strip Thin Gap Chambers (sTGCs) have been selected as one of the two detector technologies that will be used for the NSW

* Corresponding author.

http://dx.doi.org/10.1016/j.nima.2016.01.087
0168-9002/© 2016 The Authors. Published by Elsevier B.V. This is an open access article under the CC BY license (http://creativecommons.org/licenses/by/4.0/).

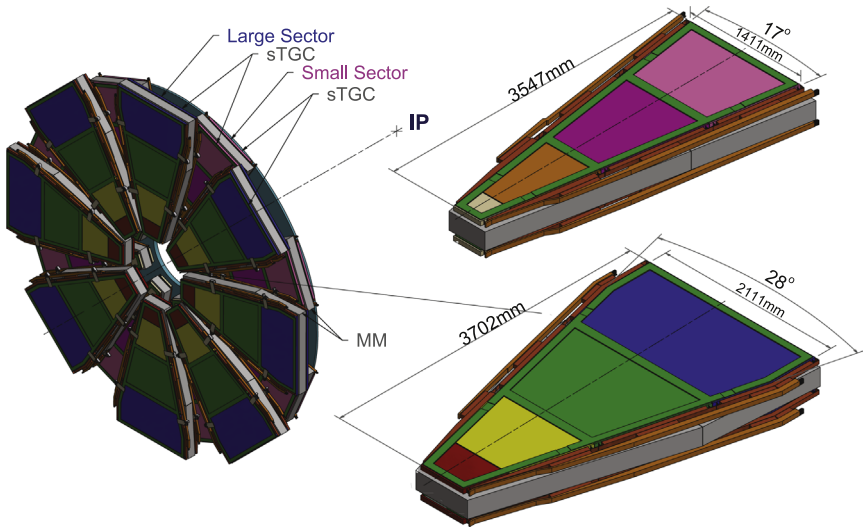

Fig. 1. Schematic diagram of the small and large sectors that make up the New Small Wheel. Each sector consists of two quadruplets of sTGC with eight micromegas (MM) detection planes in between.

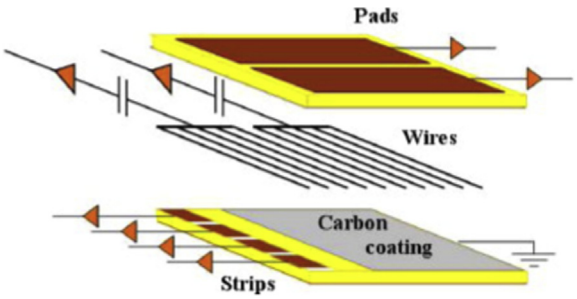

Fig. 2. Schematic diagram of the basic sTGC structure.

upgrade along with micromegas detectors. Fig. 1 shows a schematic diagram of the NSW. The NSW includes eight detection planes (layers) of sTGC arranged in two quadruplets and eight planes of micromegas. The precision reconstruction of tracks for offline analysis requires a spatial resolution of about 100 μm per sTGC layer, and the track segments have to be reconstructed online for triggering purposes with an angular resolution better than 1 mrad. A large collaboration has been established to construct these devices and is composed of members from Canada, Chile, China, Israel and Russia. These precision requirements are challenging to achieve, therefore beam test experiments have been performed to qualify the sTGC assembly procedure.

2. sTGC Technology

The concept of Thin Gap Chambers (TGCs) was developed in 1983 [5] and then used at the OPAL experiment and for the ATLAS end-cap muon trigger system. The basic sTGC structure is shown in Fig. 2. It consists of an array of 50 μm diameter gold plated tungsten wires held at a potential of 2.9 kV, with a 1.8 mm pitch, sandwiched between two cathode planes located at a distance of 1.4 mm from the wire plane. The cathode planes are made of a graphite-epoxy mixture with a typical surface resistivity of 100 or 200 kΩ/□ sprayed on a 100 or 200 μm thick G-10 plane for the inner and outer chambers, respectively. Behind the cathode planes on one side of the anode plane there are copper strips for precise coordinate measurements that run perpendicular to the wires and on the other side of the anode plane there are copper pads used for fast trigger purposes. The copper strips and pads act as readout electrodes. The pads cover large rectangular surfaces on a 1.5 mm thick printed circuit board (PCB) with the shielding ground on the opposite side. The strips have a 3.2 mm pitch, much smaller than the strip pitch of the ATLAS TGC,[1] hence the name 'small-strip TGC' for this technology. The pad occupancy for each colliding bunch of protons in the LHC is expected to be around 1.0–1.3%.

Each sTGC quadruplet consists of four pad-wire-strip planes shown in Fig. 2. The pads are used through a 3-out-of-4 coincidence to identify muon tracks approximately pointing back to the interaction point. They are also used to define a region of interest that determines which group of strips needs to be read out in order to obtain a precise position measurement in the precision coordinate, for the online track reconstruction. The azimuthal coordinate of a muon trajectory is obtained from the wires readout. The operational gas is a mixture of 55% CO_2 and 45% *n*-pentane. There are six different sizes of sTGC quadruplets, three for each of the large and small sectors. As shown in Fig. 1, all have trapezoidal shapes with surface areas between 1 and 2 m^2.

3. Construction of a large sTGC prototype

A challenge in the construction of large area multi-layer particle detectors is to achieve high precision alignment of the readout strips across layers. The required accuracy in the position and parallelism of the precision strips between planes is 40 μm. This precision is achieved by mechanical machining. The readout strips for an sTGC plane are machined together, in one step, with brass inserts which can be externally referenced. The cathode boards are glued together, separated by chamber walls at the periphery of the boards as well as 7 mm wide T-shaped wire supports and spacer buttons in approximately 20 cm intervals. The detector has been designed such that every charged particle originating from the ATLAS interaction point will traverse at most one support structure in one out of the four sTGC planes.

The resulting individual chambers are glued together, separated by a specially machined frame with a honeycomb structure over the entire surface of each chamber, which is smaller by 100 μm than the gap between chambers. The glue serves as a filler to compensate for small deviations in the thickness of the PCB material. The gluing procedure makes use of the fact that the

[1] The strip-pitch of the TGC varied between 150–490 mm.

various sTGC layers can be positioned with respect to each other with high accuracy, using the external brass inserts attached to an external precision jig on a marble table.

In the spring of 2014, the Weizmann Institute of Science in Israel built the first full-size sTGC quadruplet detector of dimensions $1.2 \times 1.0\ m^2$. This prototype consists of four sTGC strip and pad layers and is constructed using the full specification of one of the quadruplets to be used in the NSW upgrade (the middle quadruplet of the small sector).

4. Readout electronics of the sTGC prototype

A versatile application-specific integrated circuit (ASIC) is being developed to read out the pads, strips and wires of the sTGC detectors. The first prototype version of this ASIC (the so-called VMM1 [6] chip), was used to read out pads and strips at the Fermilab and CERN beam tests described below. This is the first time the VMM1 ASIC was used to measure the performance of a full-size sTGC prototype detector.

The VMM1 analog circuit features a charge amplifier stage followed by a shaper circuit and outputs the analog peak value (P) of the signal. The readout of the ASIC is zero suppressed and thus only peak values of channels with signals above a predefined threshold are read. The VMM1 may be programmed to also provide the input signal amplitude of channels adjacent to a channel above threshold (neighbour-enable logic). The VMM1 chip has the ability to read out both positive (strips, pads) and negative (wires) polarity signals, on 64 individual readout channels. The shaping amplifier features an adjustable peaking time (25, 50, 100, 200 ns) and is realized using the delayed dissipative feedback architecture which offers lower noise and higher dynamic range. The VMM1 also features an output baseline stabilizer circuit and the gain is configurable (0.5, 1.0, 3.0 and 9.0 mV/fC). An internal global DAC and a 1 pF calibration capacitor provide the ability to send test signals of different selectable charges to each individual readout channel. Finally, the VMM1 has an analog monitor output which can be programmed to output the analog waveform after the shaping stage of any of the 64 channels.

The analog signal amplitude is designed to be proportional to the input charge. An estimate of the input signal charge is therefore obtained by subtracting each channel baseline from its readout analog peak value. The average VMM1 channel baseline is approximately 180 mV with a channel-by-channel baseline variation of up to $\pm 3\%$ around the average baseline value.

The analog peak values of channels above threshold (and possibly adjacent channels) are digitized by a 13-bit ADC on a separate custom data acquisition card providing input/output Ethernet interface. Both the configuration of the VMM1 and digitized readout of the channels' peak values are transmitted over Ethernet through the custom data acquisition card.

The precise position of a charged particle traversing an sTGC gas volume can be estimated from a Gaussian fit to the measured charge on adjacent readout strips (referred to as strip-clusters from here on). Given the strip pitch of 3.2 mm and sTGC geometry, charges are typically induced on up to five adjacent strips. The spatial sampling of the total ionization signal over a small number of readout channels means that a precise knowledge of each individual readout channel baseline is necessary in order to achieve the best possible measured spatial resolution. The baseline of each individual readout channel was measured by making use of the neighbour-enabled logic of the VMM1 and its internal calibration system. Test pulses were sent on one readout channel with the neighbour-enabled logic on, and baseline values were obtained by reading out the analog peak values of the two channels adjacent to the one receiving a test pulse. Baseline values for each individual readout channel were measured and observed to be stable as a function of time (to better than 1%).

5. Position resolution measurements at Fermilab

The main goal of the beam test experiment at Fermilab was to determine the position resolution of the first full-size sTGC prototype detector. An external silicon pixel tracking system was employed to precisely characterize the sTGC performance and aid in the determination of the intrinsic spatial resolution. Previous measurements of the resolution of other sTGC prototypes, including determining the dependence of the resolution on the track incidence angle, are described in [7–9].

5.1. Experimental setup at Fermilab

In May 2014, the full-size sTGC prototype was tested with a 32 GeV pion beam at the Fermilab Test Beam Facility. The beam intensity was approximately 4000 particles per spill and corresponded to a particle rate of about 1 kHz on average with a $1\ cm^2$ beam spot size.

The beam enclosures were outfitted with laser systems that allowed the determination of the beam location in the transverse plane of the experimental setup. As shown in Fig. 3, the sTGC detector was mounted onto a motion table that was controlled remotely with a 1 mm precision. The particle beam was along the z-axis, while the sTGC detector was moved in the x- and y-directions in order to test different areas of the detector.

The sTGC was positioned between the two arms of the EUDET pixel telescope [10] as shown schematically in Fig. 4. The telescope consisted of six Minimum Ionizing MOS Active Pixel Sensor (Mimosa) planes that have a $224\ mm^2$ active area. Each arm

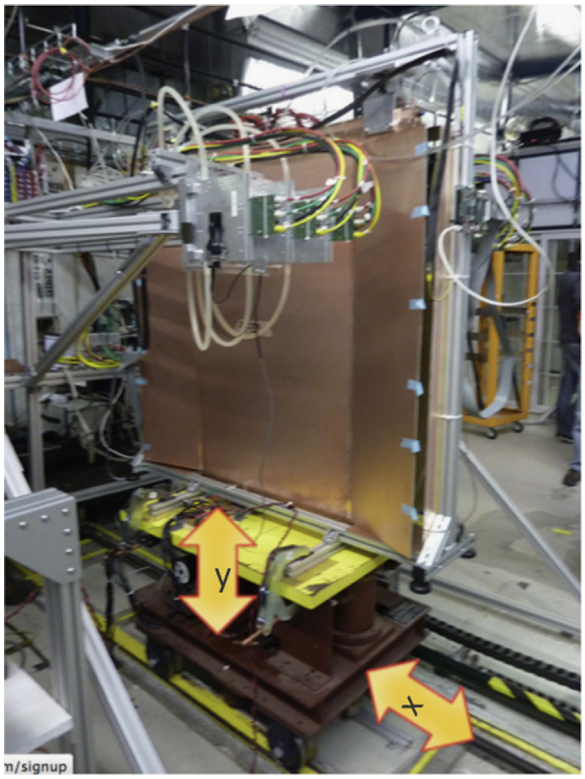

Fig. 3. Experimental setup of the beam test at the Fermilab Test Beam Facility. The sTGC prototype detector, inside a copper Faraday cage, was mounted on a motion table. Two arms of the EUDET silicon pixel telescope were positioned before and after the sTGC detector.

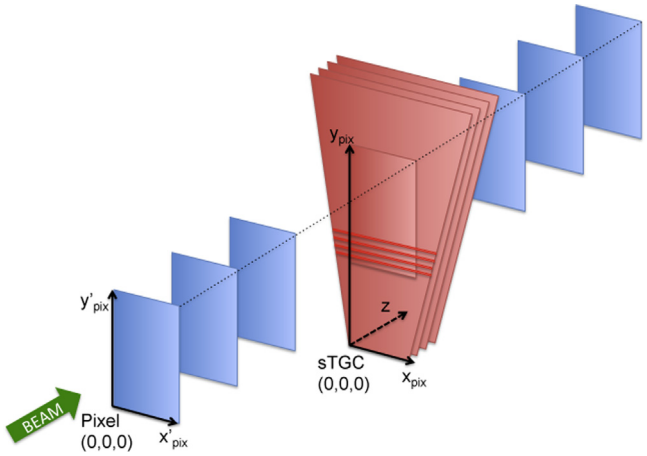

Fig. 4. Schematic diagram of the experimental setup at Fermilab and coordinate systems used. Three layers of silicon pixel sensors are positioned before and after the sTGC detector. The dimensions are not to scale.

consisted of three sensor planes. For each arm, the distance between sensor planes was about 15 cm. The two arms were separated by 64 cm. The Mimosa of the EUDET telescope offered excellent performance in terms of intrinsic resolution, material budget and readout electronics. The Mimosa26 [12] 18.4 μm pitch sensor pixel technology is based on a CMOS manufacturing process with a matrix organized in 576 rows and 1152 columns. Based on the pitch of the pixels, the single-pixel intrinsic resolution of the Mimosa26 is expected to be 5.3 μm. A better resolution was achieved from the combination of pixels into clusters. The sensor thresholds were optimized to improve the intrinsic resolution. A pointing track with precision of about 4 μm was achieved after a careful alignment of the Mimosa26 sensor planes. The EUDET telescope provided a very precise pion-trajectory reference for the sTGC detector.

Event triggering was controlled by a custom Trigger Logic Unit (TLU). The TLU received signals from two 1×2 cm^2 scintillators placed in front and behind the telescope. The TLU generated the trigger signal that was distributed to the telescope and the sTGC readout electronics. The telescope sensors were read out in a column-parallel mode with an offset-compensated discriminator to perform the analog-to-digital conversion which allowed a 115.2 μs digital binary readout. The sTGC detector was read out using the VMM1 ASIC and a custom data acquisition card. An Arduino microcontroller board [11] controlled the TLU system and cleared the latched trigger/signal busy provided by a custom I/O board necessary to achieve synchronization between the telescope and sTGC data. The data of each event were sent via Ethernet using the UDP protocol and stored on a local disk array.

The bandwidth of the EUDET readout system and of the Arduino synchronization system allowed to read out all six Mimosa26 sensors and the sTGC detector at a maximum possible rate of about 2 kHz. The silicon pixel hit positions were then used for reconstructing straight three dimensional charged-particle tracks. A track quality parameter was obtained for each fitted pion track based on the χ^2 of the track-fit. A small value of the track quality parameter corresponds to a straight track and a cut on this parameter can therefore be used to mitigate multiple scattering which are not considered in this analysis.

5.2. Analysis model

Two analyses are performed to determine the intrinsic sTGC position resolution of a single plane. In the first analysis, the intrinsic detector resolution is estimated by comparing the extrapolated beam

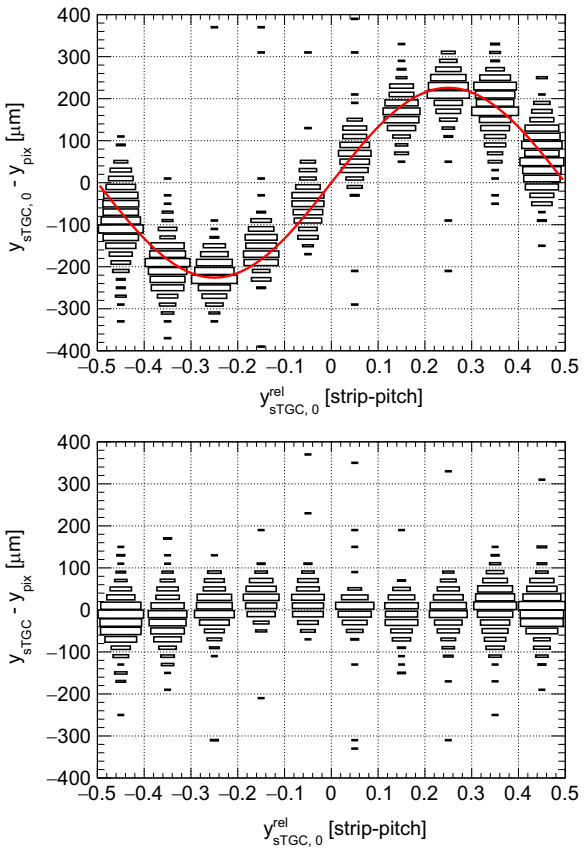

Fig. 5. The differential non-linearity for sTGC strip-clusters is shown before (top) and after the sinusoidal correction is applied (bottom).

particle trajectory reconstructed by the external silicon pixel telescope, with measurements in each of the four sTGC quadruplet planes. This analysis is referred to as the 'pixel telescope analysis' hereafter. In the second analysis, the spatial resolution is estimated based on the difference between two independent measurements of the beam particle position determined in two adjacent sTGC layers and is referred to as the 'sTGC standalone analysis'. For both analyses, the x–y plane of the coordinate system is defined as the surface of the sTGC strip layer under study. The y-axis is defined perpendicular to the strips as shown in Fig. 4. The sTGC strip-clusters therefore provide measurements of the particle position in the y-direction (y_{sTGC}) of this plane. The position resolution is directly related to the profile of induced charge on the strips. The particle position is estimated from a Gaussian fit to the induced charge distribution on the strips. The neighbour-enabled logic of the VMM1 was used. Strip-clusters with induced charge in either 3, 4 or 5 adjacent strips are selected.

For the pixel telescope analysis, the data from each of the four sTGC strip layers are analysed separately. To reduce the effect of multiple scattering on the resolution measurement, only pixel telescope tracks with track quality parameter < 10 are considered. The pixel telescope tracks provide both coordinates, x_{pix} and y_{pix} at the position of the sTGC layer studied. The spatial resolution measurement is obtained by fitting the residual distribution $y_{\mathrm{sTGC}} - y_{\mathrm{pix}}$ with a Gaussian model.

The charge measured on the strips of the sTGC detector results from a spatial sampling and discretization of the induced charge. The process of reconstructing the sTGC strip-cluster position from this sampling introduces a differential non-linearity effect on the reconstructed strip-cluster position. The deviation of the measured strip-cluster position from the expected position (estimated by the pixel telescope track) depends on the strip-cluster position relative to the strips. This dependence is clearly seen in the two-

Table 1
Amplitude parameter a_i for the differential non-linearity correction for three sTGC strip-cluster multiplicities.

Strip-cluster multiplicity i	Amplitude parameter a_i
3	205 ± 9
4	206 ± 4
5	211 ± 5

dimensional distributions in Fig. 5 (top). It shows the y-residual versus strip-cluster position relative to the closest inter-strip gap centre $y^{\mathrm{rel}}_{\mathrm{sTGC},\,0}$. This effect is corrected using a sinusoidal function according to:

$$y_{\mathrm{sTGC}} = y_{\mathrm{sTGC},\,0} - a_i \sin\left(2\pi\, y^{\mathrm{rel}}_{\mathrm{sTGC},\,0}\right) \quad (1)$$

where $y_{\mathrm{sTGC},\,0}$ is the strip-cluster mean resulting from the Gaussian fit and y_{sTGC} is the corrected particle position estimator. The amplitude parameters are denoted a_i for the 3, 4 and 5 strip-multiplicity categories; the index i denotes the corresponding category. These amplitude parameters are free parameters in the fit. The values of the amplitude parameters obtained from the fit to data are compatible with being equal for the three strip-cluster multiplicities as shown in Table 1. The correction function is therefore universal and is shown in Fig. 5 (top). The two-dimensional distribution after the correction is applied was found to be reasonably flat as shown in Fig. 5 (bottom).

The alignment of the coordinate system of the pixel telescope with respect to the above-defined coordinate system of the sTGC layer also affects the measured residual distribution. A simple two-parameter model is used to account for translations and rotations of the two coordinate systems with respect to each other. Both the alignment correction and the differential non-linearity correction are included *in situ* in the analysis. The alignment correction is introduced in the model by expressing the pixel track position in the sTGC-layer coordinate system y_{pix}, as a function of the track position in the pixel telescope coordinate system x'_{pix} and y'_{pix}, and two misalignment parameters δy and ϕ_{xy}, as follows:

$$y_{\mathrm{pix}} = -x'_{\mathrm{pix}} \sin\phi_{\mathrm{xy}} + y'_{\mathrm{pix}} \cos\phi_{\mathrm{xy}} + \delta y. \quad (2)$$

The variable δy corresponds to a misalignment along the y-axis of the sTGC coordinate system, and ϕ_{xy} corresponds to a rotation of the telescope coordinate system in the x–y plane around the z-axis of the sTGC coordinate system. Translation and rotation misalignments along and around the other axes are not taken into account in this model, since they are expected to have a small impact on the determination of the intrinsic position resolution. Fig. 6 shows the two-dimensional distribution of y-residual versus x'_{pix} for a representative data-taking period (run) and sTGC strip-layer. In the top figure the rotation alignment correction has been omitted when computing y-residuals. The mean of the residual distribution increases linearly as a function of x'_{pix}, which is evidence for a small rotation between the two coordinate systems. The red line represents the correction applied to this dataset. Accounting for this correction results in a distribution that is independent of x'_{pix} as shown in Fig. 6 (bottom).

The global model fitted to the data is the following double Gaussian function:

$$F_i = F_i(y_{\mathrm{sTGC},\,0},\, y^{\mathrm{rel}}_{\mathrm{sTGC},\,0},\, x'_{\mathrm{pix}},\, y'_{\mathrm{pix}};\, \delta y,\, \phi_{\mathrm{xy}},\, a_i, \sigma, f,\, \sigma_{\mathrm{w}})$$
$$= f\, G(y_{\mathrm{sTGC}} - y_{\mathrm{pix}};\, 0,\, \sigma) + (1-f)\, G(y_{\mathrm{sTGC}} - y_{\mathrm{pix}};\, 0,\, \sigma_{\mathrm{w}});$$

where G denotes a Gaussian function. The parameter f determines the relative normalization of these two Gaussian functions. The value of f represents the fraction of the data parameterized by the narrow Gaussian and it is typically around 95% with a RMS of about 2%. The first Gaussian represents the core of the residual distribution. The width parameter σ is the parameter of interest for the determination of the intrinsic position resolution.

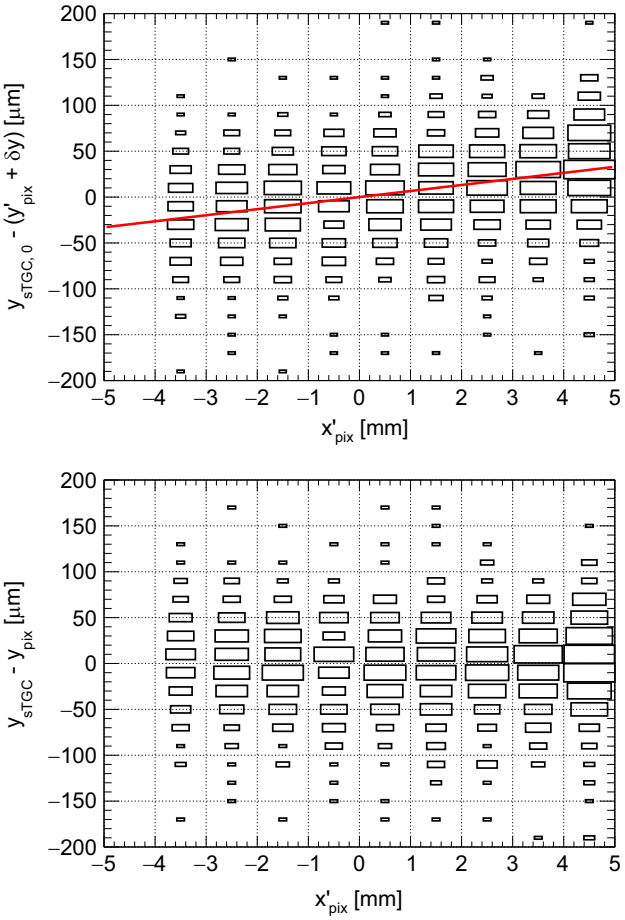

Fig. 6. Two-dimensional distribution of y-residual versus x'_{pix} for a representative data taking run and sTGC strip-layer. For the top figure the rotation alignment correction (red line) has been omitted when computing y-residuals, whereas the bottom figure shows the corrected y-residual distribution.

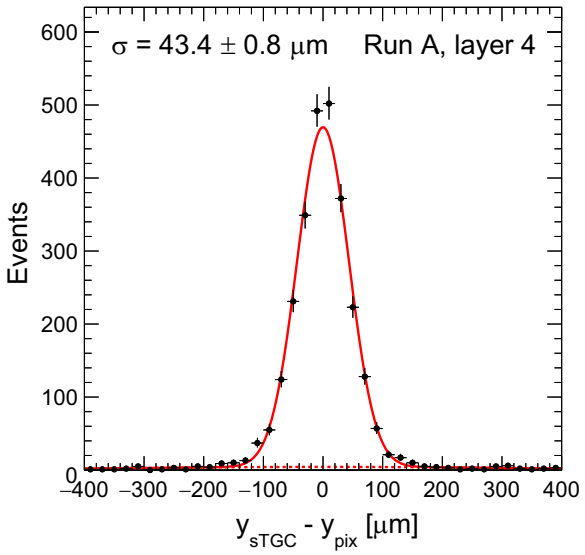

Fig. 7. The residual distribution after all corrections are applied together with the result for the intrinsic resolution parameter σ for Run A, strip-layer 4.

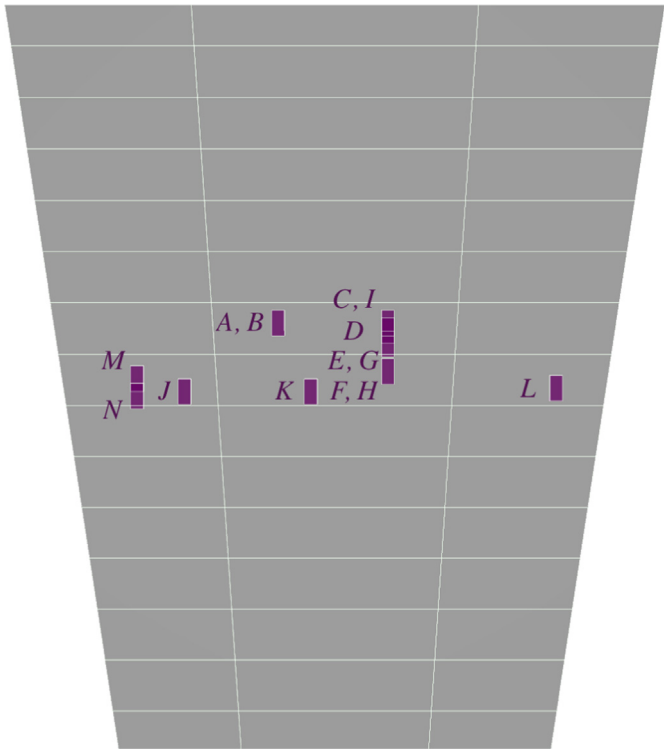

Fig. 8. Summary of the beam positions with respect to the sTGC detector for various data taking runs during the beam tests at Fermilab.

A wider Gaussian of width parameter σ_w covers reconstructed strip-clusters from background sources. The residual distribution $y_{sTGC} - y_{pix}$ is shown in Fig. 7 together with the result for the intrinsic resolution parameter σ for a representative data taking run and sTGC strip-layer.

For the sTGC standalone analysis, the sTGC strip-cluster positions are corrected for the differential non-linearity obtained from the pixel telescope analysis. Assuming the two sTGC strip-layers to be identical, the position resolution of a single layer σ can be estimated from the width of the distribution of pairwise sTGC strip-layer position residuals $\sigma = \sigma_{residual}/\sqrt{2}$.

5.3. Intrinsic position resolution

The determination of the intrinsic sTGC position resolution described in the previous section is applied to data accumulated during several data taking runs. Using the motion table on which the sTGC detector was mounted, the position of the sTGC detector was varied in the two dimensions perpendicular to the pion beam. Fig. 8 shows the beam positions for various data taking runs. A large area of about 65×12 cm^2 of the sTGC detector was exposed to the pion beam, enabling a test of the homogeneity of the detector.

The intrinsic position resolution of each sTGC strip-layer in the sTGC quadruplet was measured using the pixel telescope analysis. For each data taking run, the same pixel telescope tracks are used to determine the intrinsic resolution in each of the four sTGC strip-layers. The results for Runs A–F are shown in Fig. 9.

The resolution measurements in the first sTGC strip-layer is larger for all runs because the individual readout channel baseline correction was not available. The analysis of Run E revealed that the beam crossed an internal mechanical support structure in strip-layers two (wire support) and layer three (spacer button) of the sTGC detector. The largest degradation in resolution, to about 80 μm, is observed in layer-2 for Run E. The resolution

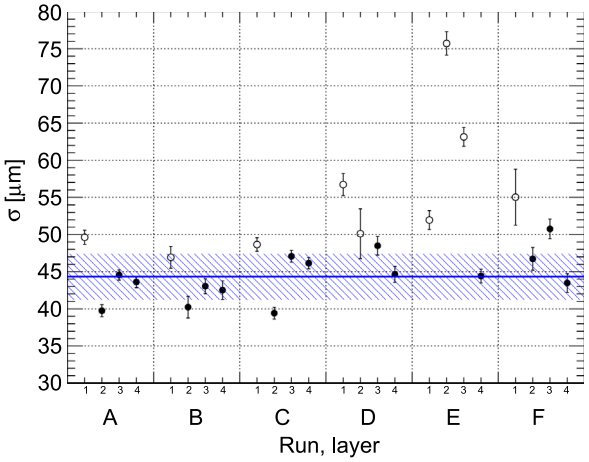

Fig. 9. Summary of the measured intrinsic sTGC resolution using the pixel telescope analysis for different data taking runs. The beam position on the sTGC detector for each run is shown in Fig. 8. Results for runs with no expected degradation due to sTGC detector support structure or calibration are shown as black filled circles. The horizontal line represents the average resolution for these runs whereas the hashed band represents the RMS spread. Results for the remaining runs are shown as open circles.

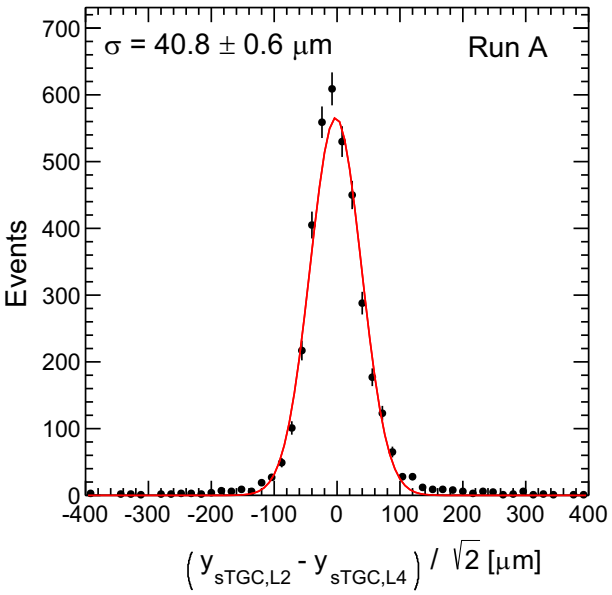

Fig. 10. Resolution estimate based on adjacent sTGC strip-layer position residual distributions for a representative sTGC standalone data taking run.

measurements for configurations with expected degradation due to sTGC support structure or missing readout channel baseline correction are shown as open circles in Fig. 9. All measurements with good configurations are shown as black filled circles. The average of these measurements is about 45 μm with an RMS spread of 8 μm. The largest source of systematic uncertainty in this analysis is assumed to originate from multiple scattering. The magnitude is about 6 μm, estimated from the dependence of the measured sTGC position resolution on the pixel telescope track quality parameter cut. The results are well below 100 μm and therefore meet the ATLAS requirement for the NSW upgrade project.

For Runs G–I, no synchronized pixel telescope and sTGC data were available. The analysis of these runs revealed that the pion beam crossed the wire support structure in at least one of the sTGC layers of the quadruplet. Here the resolution is estimated

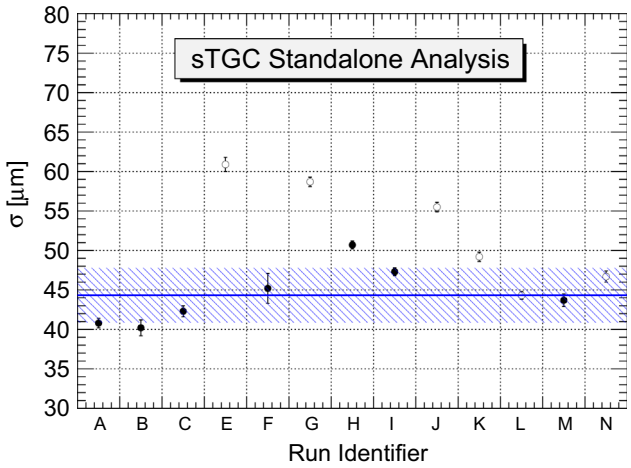

Fig. 11. Summary of the measured intrinsic sTGC resolution using the sTGC standalone analysis for different data taking runs. The beam position on the sTGC detector for each run is shown in Fig. 8. Results for runs with no expected degradation due to sTGC detector support structure or calibration are shown as black filled circles. The horizontal line represents the average resolution for these runs whereas the hashed band represents the RMS spread. Results for the remaining runs are shown as open circles.

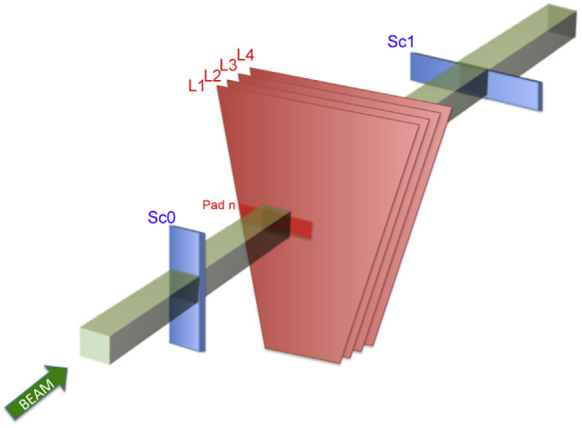

Fig. 12. Schematics of the experimental setup of the CERN beam test experiment. Two scintillators are positioned perpendicular to each other, one before and one after the chamber, which define a coincidence area of 12×12 cm^2, centred on pad n.

using the sTGC standalone analysis. The resolution is shown in Fig. 10 for a representative sTGC standalone run. A summary of the measurements for all runs is shown in Fig. 11. Measurements for configurations with expected degradation due to sTGC detector support structure or calibration are shown as open circles. The measurement with no expected degradation is shown as black filled circles. The weighted average of these measurements is also about 45 μm, consistent with the pixel telescope analysis, with a spread of 8 μm.

6. Pad readout measurements at CERN

A test beam experiment was conducted at the CERN H6 facilities, using a 130 GeV muon beam of about 4 cm radius, to test the characteristics of the pads. The setup is shown in Fig. 12. The system was triggered by a set of scintillators with a 12×12 cm^2 coincidence area.

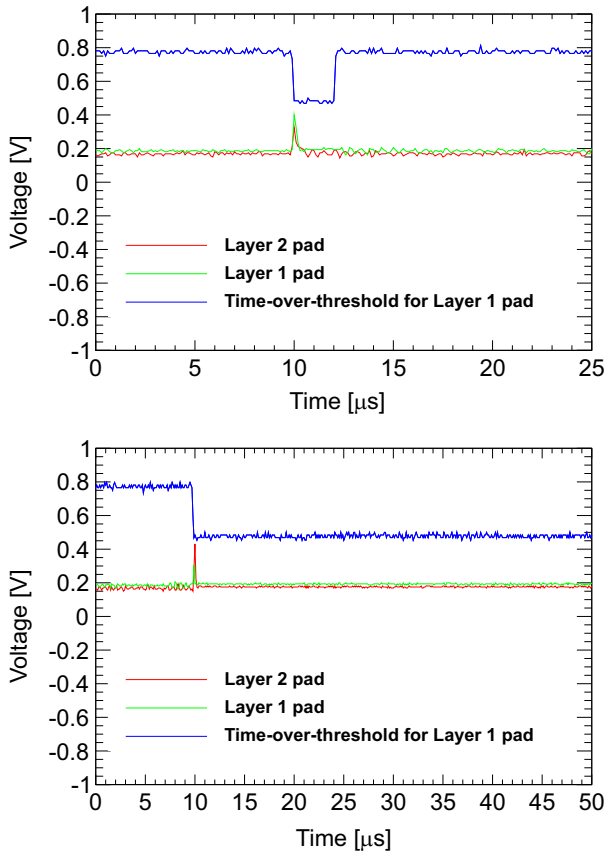

Fig. 13. Oscilloscope event examples, where the amplifier shows a short dead time (top) and where the dead time lasted for tens of microseconds (bottom).

6.1. Deadtime and efficiency measurements

The preliminary front-end electronics based on the VMM1 ASIC is not yet well adapted to the arrival of small late charges from the sTGC detector, when using the present default configurations. This can lead to large dead time in its response, which in turn leads to an inefficiency of the system when running at high rate (typically 80–90% efficiency at 100 Hz/cm^2). The final VMM electronics will provide the required signal processing capabilities to address this issue.

To ensure that no inefficiency was due to the detector itself, the large cathode pads were used to estimate the detector efficiency, which was measured by looking at the analog output of the front-end amplifier. The efficiency of pad n in the first layer was defined with respect to the coincidence of the trigger with a signal in the fully overlapping pad of the second layer.

Fig. 13 shows two typical analog pulses: one where the amplifier shows a short dead time following the detector signal (top), and one where the dead time lasted for tens of microseconds (bottom). By recording hundreds of triggered events using an oscilloscope, the presence of a detector signal within the live-part of the front-end electronics (independent of the signal threshold) was checked. This test confirmed that the detector was 100% efficient.

By placing the beam and a scintillator coincidence triggering area of 12×1 cm^2 centred on a single 8×60 cm^2 pad and looking at the signal in neighbouring pads, one could determine that any cross-talk to neighbouring pads does not exceed 5% of the cases. This should be considered as an upper limit since the muon beam did contain also two muons per event, where the second muon could be outside the region that was instrumented with strip-readout electronics.

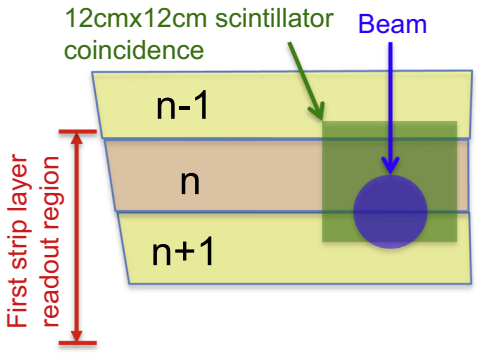

Fig. 14. Schematics of the experimental setup for charge sharing measurements. The beam and the scintillator coincidence area cover the transition between pad n and pad $n+1$.

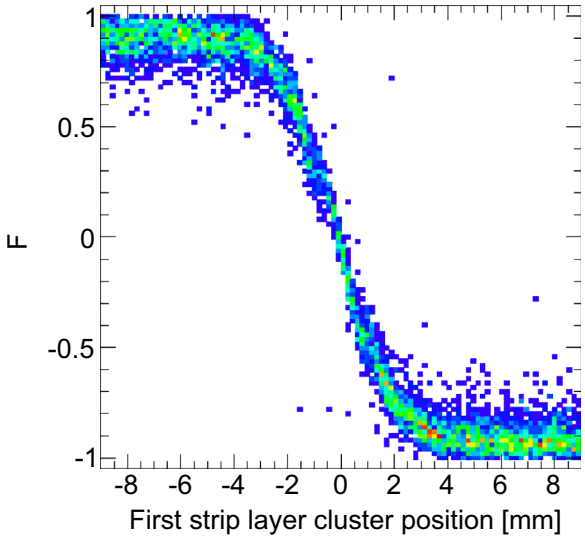

Fig. 15. Fraction of the charge collected by pad n as a function of the position with respect to the centre of the transition region. F=1 implies all the charge is deposited in pad n, while F=-1 means all the charge goes to pad $n+1$.

6.2. Charge sharing between pads

To study the transition region between pads, the scintillator coincidence triggering area and the particle beam were centred between pad n and pad $n+1$ of the first layer, as illustrated in Fig. 14.

After applying timing quality requirements on the strip and pad hits, the channel baseline values are subtracted from the analog peak values. Strip-clusters with induced charge in either 3, 4 or 5 adjacent strips are selected and calibrated in the same way as for the Fermilab beam test. Events with a single strip-cluster in the first layer and the second layer are selected. The strip-cluster position (mean of the fitted Gaussian) in the first layer is used to define the position of the particle going through the detector. The events are further required to contain a hit above threshold on either pad n or pad $n+1$. The charge fraction (F) is defined using the analog peak values (P) of the two adjacent pads:

$$F = \frac{P_n - P_{n+1}}{P_n + P_{n+1}} \quad (3)$$

Fig. 15 shows the charge fraction as a function of the position with respect to the centre of the transition region between the pads. It shows that the transition region, where the two pads share more than 70% of the induced charge, spans about 4 mm.

7. Conclusions

The spatial resolution for a full-size sTGC prototype detector for the ATLAS NSW upgrade has been measured in a 32 GeV pion beam test experiment at Fermilab. A six-layer silicon pixel telescope has been employed to characterize the sTGC detector and to correct for differential non-linearity of the reconstructed sTGC strip-cluster position. At perpendicular incidence angle, single strip-layer position resolutions of better than 50 μm have been obtained, uniform along the sTGC strip and perpendicular wire directions, well within design requirements. The characteristics of the sTGC pad readout have been measured in a 130 GeV muon beam test at CERN. The transition region between readout pads has been found to be 4 mm, and the pads have been found to be fully efficient.

Acknowledgements

The authors would like to thank the members of the NSW collaboration for their contributions and in particular the NSW electronics group for providing the VMM1 based readout system. We would also like to thank B. Iankovski, F. Balahsan, G. Cohen, S. Sbistalnik, A. Klier from the Weizmann Institute of Science, M. B. Moshe from Tel-Aviv University, M. Batygov, M. Bowcock, Y. Baribeau, P. Gravelle from Carleton University, R. Openshaw from TRIUMF and J. Fried from BNL for supporting this work. We are also thankful to the firm MDT SRL (Milan) for their efforts in producing the first prototypes of large cathode boards, which made the construction of the tested module possible. We acknowledge the support of of the Israeli Science Foundation (ISF), CIRP-Israel-China Collaboration Grant 549/13, the MINERVA foundation – project 711143, the Benoziyo Center for Particle Physics, the Natural Sciences and the Engineering Research Council (NSERC) of Canada and CONICYT, Chile.

References

[1] ATLAS Collaboration, Journal of Instrumentation 3 (2008) S08003.
[2] ATLAS Collaboration, ATLAS Muon Spectrometer Technical Design Report, CERN/LHCC 97–22, 1997.
[3] ATLAS Collaboration, *New Small Wheel Technical Design Report*, CERN-LHCC-2013-006, 2013.
[4] HL-LHC Collaboration, *The High Luminosity LHC Project*, ⟨http://hilumilhc.web.cern.ch/about/hl-lhc-project⟩.
[5] S. Majewski, et al., Nuclear Instruments and Methods in Physics Reasearch A 217 (1983) 265.
[6] G. De Geronimo, et al., IEEE Transactions of the Nuclear Science NS-60 (3) (2012) 2314.
[7] V. Smakhtin, G. Mikenberg, A. Klier, et al., Nuclear Instruments and Methods in Physics Research A 598 (2009) 196.
[8] G. Mikenberg, D. Milstein, V. Smakhtin, et al., Nuclear Instruments and Methods A 628 (2011) 177.
[9] G. Mikenberg, D. Milstein, V. Smakhtin, et al., Test of special resolution and trigger efficiency of a combined Thin Gap and Fast Drift Tube Chambers for high luminosity LHC upgrades, 2011 IEEE Nuclear Science Symposium Conference Record NP5.S-200.
[10] I. Rubinskiy, *An EUDET/AIDA pixel beam telescope for detector development*, Proceedings of the 2nd International Conference on Technology and Instrumentation in Particle Physics (TIPP 2011), vol. 37, 2012, pp. 923–931.
[11] Arduino, *UNO*, ⟨https://www.arduino.cc/en/Main/arduinoBoardUno⟩.
[12] C. Hu-Guo, et al., Nuclear Instruments and Methods in Physics Research A 623 (2010) 480.